



## **Cold-formed steel strength predictions for combined bending and torsion**

Yu Xia<sup>1</sup>, Robert S. Glauz<sup>2</sup>, Benjamin W. Schafer<sup>3</sup>, Michael Seek<sup>4</sup>, Hannah B. Blum<sup>5</sup>

### **Abstract**

Locally slender cross-section members, such as cold-formed steel Cee and Zee sections, are susceptible to significant twisting and high warping torsion stresses. Torsion considerations are complicated by whether it is derived as a first-order effect from loading or a second-order effect from instability. The current design for combined bending and torsion interaction has some limitations, including only considering the first yield in torsion and ignoring the cross-section slenderness in torsion. Previous work has derived a simple uniform equation to predict the bimoment capacity and two bimoment strength curves for local and distortional buckling under torsion only. This work is extended to consider combined bending and torsion for locally slender cross-sections. A parametric study is conducted to improve the interaction prediction of combined bending and torsion for a range of torsional slenderness. Shell finite element analysis of lipped Cee and Zee section members with combined bending and torsion were created using a validated model. A practical range of cross-sections and bracing conditions were investigated with various ratios of applied torsion and bending. Shell finite element buckling and collapse analyses were performed to determine the critical and ultimate moments and bimoments. It was found that the current AISI standard is conservative under most scenarios. Updated torsion-bending interaction equations incorporating bimoment and bending moment are proposed. The interaction equations are dependent on the cross-section, the direction of the applied torsion, and the bracing condition.

### **1. Introduction**

Cold-formed steel (CFS) is a common construction material in which steel sheets are shaped into structural members by the cold-working processes and are widely used in many structural and non-structural applications. Among different types of CFS shapes, the thin-walled open sections (e.g., Cee and Zee) are the most common for structural framing. The thin-walled geometries are beneficial to reducing the self-weight, hence lower transportation, material costs, and labor costs. However, due to the open thin-walled geometries, CFS sections have a low torsional stiffness and

---

<sup>1</sup>Assistant Professor, China University of Geosciences (Beijing), <xiayu@cugb.edu.cn>; formerly PhD Candidate, University of Wisconsin-Madison

<sup>2</sup>President/Owner, RSG Software, Inc., <glauz@rsgsoftware.com>

<sup>3</sup>Professor, Johns Hopkins University, <schafer@jhu.edu>

<sup>4</sup>Associate Professor, Old Dominion University, <mseek@odu.edu>

<sup>5</sup>Assistant Professor, University of Wisconsin-Madison, <hannah.blum@wisc.edu>

can be vulnerable to even a small amount of torsional load. Therefore, understanding the internal torsional forces for CFS members is important to correctly conduct the member and structure design (Glauz, 2020).

A member subjected to torsional loads may develop both shear stresses and longitudinal stresses. For typical open cross sections, the most critical internal force is the bimoment ( $B$ ) caused by the longitudinal stresses. However, in the literature there is limited guidance on methods to calculate the bimoment strength and a few design standards provide only indirect methods to consider the effects resulting from torsional stresses. Section H4 of AISI S100 (2020) states that for members under combined bending and torsion, the flexural strength should be reduced by a reduction factor  $R$ , which is given as Eq. 1:

$$R = \frac{f_{bending,max}}{f_{bending} + f_{torsion}} \quad (1)$$

where  $f_{bending,max}$  is the bending stress at extreme fiber,  $f_{bending}$  is the bending stress at location in cross-section where combined bending and torsion stress is maximum, and  $f_{torsion}$  is the torsional warping stress at location in cross-section where combined bending and torsion stress is maximum.

Section 6.1.6 of Eurocode 3 Part 1-3 (2006) stipulates the upper bound of the total longitudinal stress and the total shear stress for members under combined bending and torsion as shown in Eq. 2:

$$\sqrt{\sigma_{tot,Ed}^2 + 3\tau_{tot,Ed}^2} \leq 1.1 \frac{f_{ya}}{\gamma_{MO}} \quad (2)$$

where  $\sigma_{tot,Ed}$  is the design total direct stress, calculated on the relevant effective cross-section,  $\tau_{tot,Ed}$  is the design total shear stress, calculated on the gross cross-section,  $f_{ya}$  is the steel average yield strength, and  $\gamma_{MO}$  is a safety factor.

Section 5.3.2 of GB 50018 (2002, Chinese version) stipulates the upper bound of the sum of normalized bending moment and bimoment as shown in Eq. 3, which is transformed into Eq. 4 by Wan et al. (2021):

$$\sigma = \frac{M}{W_{enx}} + \frac{B}{W_{\omega}} \leq f \quad (3)$$

$$\frac{M}{M_b} + \frac{B}{B_y} \leq 1 \quad (4)$$

where  $M_b$  is the bending capacity under bending moment only and  $B_y$  is the bimoment capacity under torsion only.

These standards consider the reduction for yield moment and bimoment, while member inelastic behaviors are not sufficiently considered.

The authors carried out a numerical study (Xia et al., 2022) to predict the bimoment capacity of thin-walled CFS Cee and Zee sections under torsional load. A uniform equation (Glauz and Schafer, 2022) consisting various bimoment parameters with only two numerical coefficients was adopted for the bimoment strength calculation as shown in Eq. 5:

$$B_n = B_p \cdot \frac{B_{cr} + aB_y}{B_{cr} + bB_y} \quad (5)$$

where  $B_y$  is the yield bimoment,  $B_p$  is the plastic bimoment, and  $B_{cr}$  is the buckling bimoment. The calculation of these bimoment parameters is introduced in the torsion-only study (Xia et al., 2022). In addition, local buckling (LB) and distortional buckling (DB) controlled cases showed substantially different behaviors and two groups of numerical coefficients were provided respectively, where  $a = 0.094$  and  $b = 0.230$  for LB-controlled cases,  $a = 0$  and  $b = 1.110$  for DB-controlled cases.

In this paper, a numerical study is carried out to predict the moment-bimoment interactions of thin-walled CFS Cee and Zee sections under combined bending-torsion. A validated finite element model (Xia et al., 2022) is updated to adapt the combined bending-torsion load scenario. Various eccentricities from the cross-section shear center to the vertical applied loads are considered. In addition, both braced and unbraced midspan conditions are investigated. Moment and bimoment parameters incorporated in the interaction equations are calculated based on the member length, cross section geometry, and simulation results. Simple interaction equations between moment and bimoment parameters are provided, where different coefficients are calibrated for unbraced or braced conditions and Cee or Zee sections, respectively.

## 2. Finite element model design

The validated Abaqus (2016) finite element model designed in the torsion-only study (Xia et al., 2022) based on the selected experimental study (Wan, Huang, and Mahendran, 2021) was adapted to investigate the behaviors of CFS under combined bending-torsion. Identical cross-section selection (Table 1), initial geometric imperfections, model element type, and model mesh size defined in the torsion-only study (Xia et al., 2022) were adopted in this study. For the material definition, an elastic-perfectly-plastic model for conventional mild steel with a yield strength of 345 MPa (50 ksi) for Cee sections and 379 MPa (55 ksi) for Zee sections were adopted.

For the applied loads, compared with the torsion-only study (Xia et al., 2022), vertical distributed loads  $p$  representing the primary bending force were added at each node of the web, while the horizontal distributed loads  $q$  representing the torsional load effect were applied at all nodes of both top and bottom flanges as shown in Figs. 4 and 5. The relationship between total vertical load  $P$  and the total equivalent transverse load  $Q$  was determined by the loading eccentricity from the shear center through the relationship  $Q = P(ds + e)/D_0$ , where  $e$  is the eccentricity from shear center,  $ds$  is the distance between the web center and the shear center, and  $D_0$  is the out-

Table 1: Selected cross-sections for the parametric study.

<b>Cee cross-section</b>			
1200S300x97 <sup>1</sup>	1000S300x97	800S250x97	600S200x97
1200S300x68	1000S300x68	800S250x68	600S200x68
1200S300x54	1000S300x54	800S250x54	600S200x54
<b>Zee cross-section</b>			
12Z325x105 <sup>2</sup>	10Z325x105	8Z275x105	6Z225x105
12Z325x070	10Z325x070	8Z275x070	6Z225x070
12Z325x059	10Z325x059	8Z275x059	6Z225x059

<sup>1</sup> The nomenclature of Cee sections can be found in SSMA Product Technical Guide (2015);

<sup>2</sup> The nomenclature of Zee sections can be found in AISI Cold-Formed Steel Design Manual (2017).

to-out web depth, as illustrated in Fig. 1. The vertical load on each node  $p$  can be calculated by  $p = P/[(n_L + 1)(n_D + 1)]$ , where  $n_L$  is the number of elements along the member longitudinal direction and  $n_D$  is the number of cross-section web elements. The horizontal load on each node is  $q = P(e + ds)/[D_0(n_L + 1)(n_B + 1)]$ , where  $n_B$  is the number of elements of either flange of the cross-section, and  $ds$  is negative for Cee sections and zero for Zee sections.

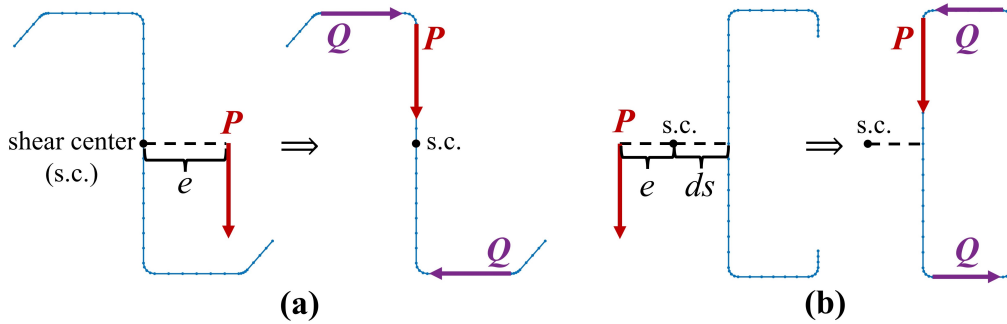


Figure 1: Transformation of eccentrically load for (a) Zee section and (b) Cee section.

For the boundary conditions, both unbraced and braced midspan conditions were investigated, where their *theoretical* moment and bimoment distributions along the member span can be calculated (Glauz, 2020) as shown in Fig. 2, and where the coordinate system is defined in Figs. 4 and 5. For both unbraced and braced cases, the member ends were simply supported, where the displacements along the Y and Z directions were restrained providing torsionally fixed but warping free boundary conditions at the ends. For the unbraced case, only the displacement along the X direction was restrained at midspan. For the braced case, the X and Z direction displacements and the rotation about the X-axis were restrained at midspan.

For comparison between the unbraced and braced cases, a design of the same torsionally unbraced length  $L$  is helpful, where  $L = L_0$  for the unbraced case and  $L = L_0/2$  for the braced case, where  $L_0$  is the total member length. Meanwhile, considering the beam length is usually dependent on the section web depth, the member length was selected as  $10D_0$  for the unbraced case and  $20D_0$  for the braced case. For both cases, up to nine different eccentricities were selected and are shown in Fig. 3, where  $B$  is the flange element flat width. Fig. 4 and 5 provide typical finite element setup for unbraced and braced cases, respectively.

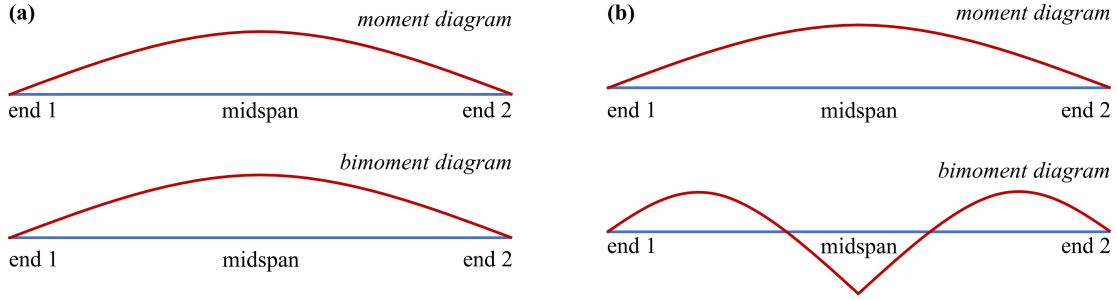


Figure 2: Theoretical moment and bimoment distribution along member length for (a) the unbraced condition and (b) the braced condition.

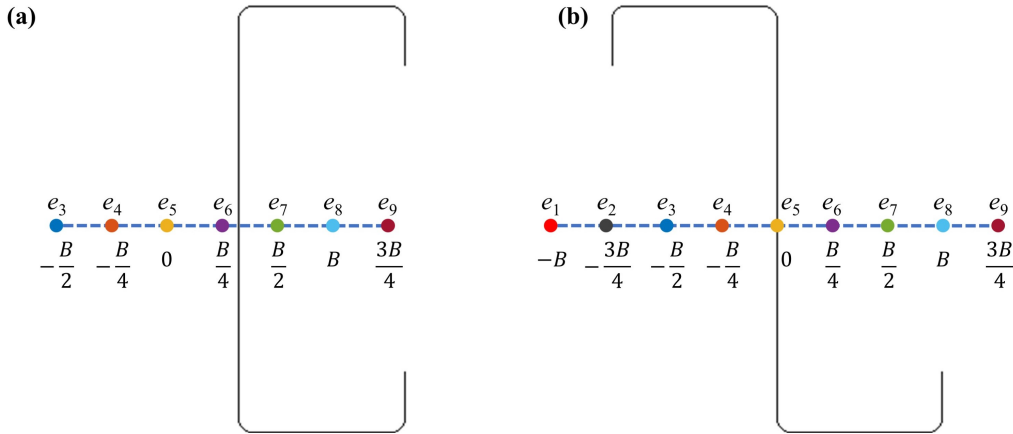


Figure 3: Selected eccentricities from shear center (location 5,  $e_5$ ) for (a) Cee and (b) Zee sections for the combined bending-torsion analysis.  $B$  is the flange element flat width.

### 3. Model collapse modes

Significantly different stress distributions at peak applied load for the two loading eccentricity direction scenarios (i.e., sign of eccentricity in Fig. 3) were observed for both unbraced Zee and Cee sections. Representative longitudinal stress (S11) distributions for unbraced Cee and Zee sections for the two eccentricity directions are shown in Figs. 6 and 7, where the most significant stress concentrations were observed at the midspan for all cases. Specifically, for Cee sections with negative load eccentricity (Fig. 6(a)), high tension on the bottom lip and high compression at the top lip were observed. For Cee sections with positive load eccentricity (Fig. 6(b)), high tension at the top lip, web, and bottom flange, particularly the web-bottom flange junction, were observed, and high compression at the top flange and the upper web were observed. For Zee sections with negative load eccentricity (Fig. 7(a)), significant compression was observed at the upper web and web-top flange junction, and high tension was observed at the top lip. For the Zee sections with positive load eccentricity (Fig. 7(b)), significant tension was observed at the web-bottom flange junction and the lower web, while significant compression was found at the bottom lip and top flange-top lip junction.

For the braced Cee and Zee sections with both negative and positive applied load eccentricities, the general distribution of S11 was similar, where the upper half of the cross-section was overall in

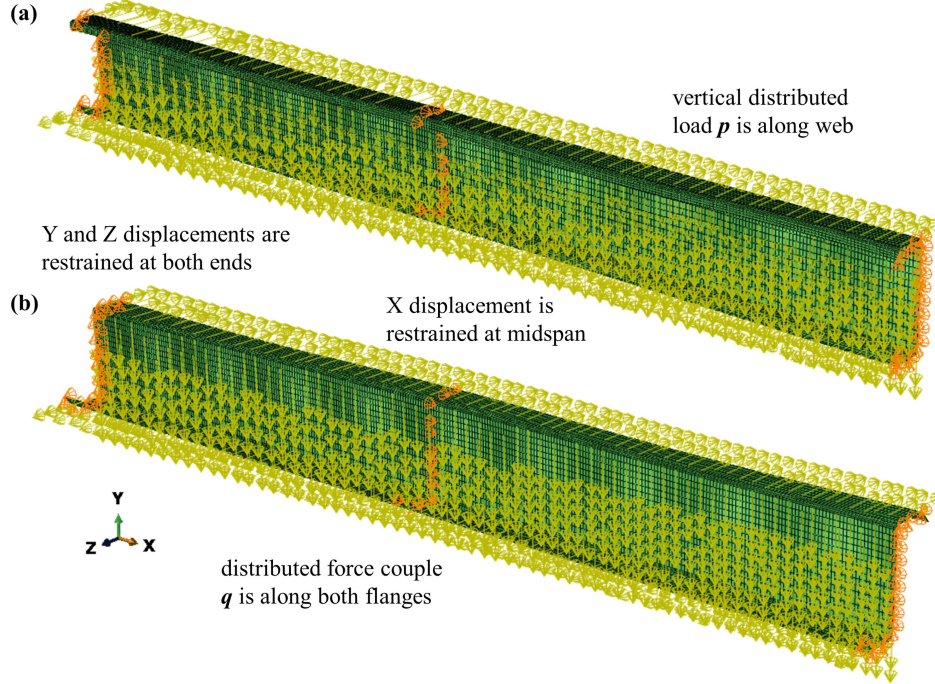


Figure 4: Typical simulation setup with unbraced midspan for (a) Cee and (b) Zee sections under combined bending-torsion loading condition. Yellow arrows are nodal loads and orange cones are displacement fixities.

compression and the lower half was overall in tension. However, the detailed S11 distribution and magnitudes were unique for each case. Specifically, comparing the two examples shown in Figs. 8 and 9, the largest compression was found at web-top flange junction and the largest tension was found at web-bottom flange junction for Cee sections with negative load eccentricities (Fig. 8(a)); while for Cee sections with positive load eccentricities (Fig. 8(b)), the largest compression was found at the top lip and the largest tension was found at the bottom lip. For the Zee sections, the compression at the top lip was most significant and no tension yield was observed when the loading was applied at  $e_1 = -B$  (Fig. 9(a)). When the eccentricity increased, the compression at the upper half of the section decreased and the tension at the lower half section increased. At  $e_9 = B$  (Fig. 9(b)), significant tension was observed at the bottom lip, while no compression beyond yield was observed in the upper half of the section. The different behaviors for unbraced and braced Cee and Zee sections might indicate different moment-bimoment interactions for these cases.

#### 4. Parameter calculation

To develop the interaction between moment and bimoment parameters for the combined bending-torsion case, the calculation of the following parameters are required: nominal moment capacity  $M_n$ , the ultimate moment  $M_u$ , the nominal bimoment capacity  $B_n$ , and the ultimate bimoment  $B_u$ .

To calculate  $M_u$  and  $B_u$ , the peak applied load and/or the nodal longitudinal stress (S11) at peak load extracted from the finite element analysis are needed. Two methods were adopted for the calculations. The first method directly calculated  $M_u$  and  $B_u$  based on elastic distribution equations using the applied ultimate loads.  $M_u$  for unbraced Cee sections is calculated by Eq. 6:

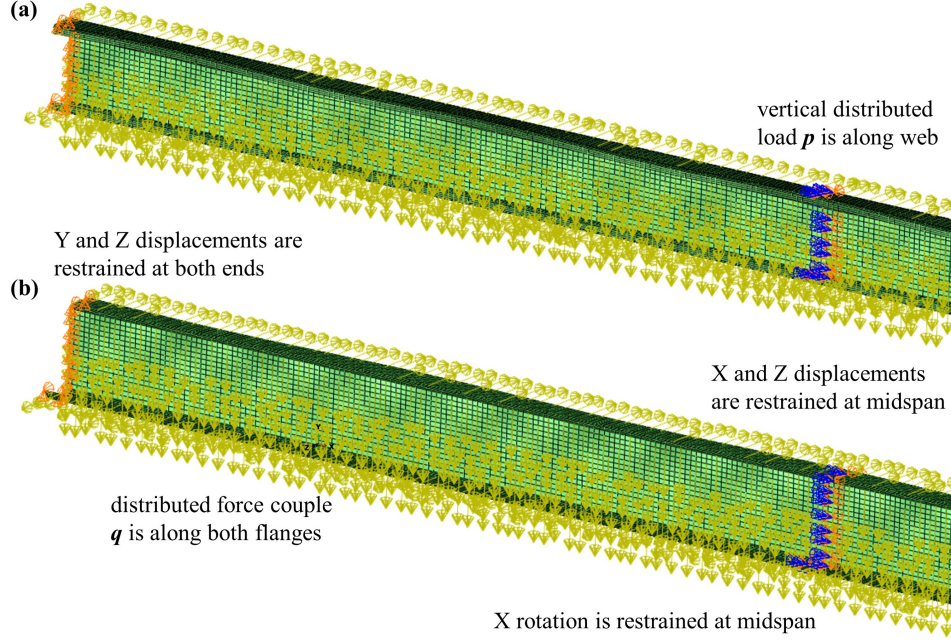


Figure 5: Typical simulation setup with braced midspan for (a) Cee and (b) Zee sections under combined bending-torsion loading condition. The right half (not shown) is symmetric with the left half about the midspan. Yellow arrows are nodal loads, orange cones are displacement fixities, and blue cones are rotation fixities.

$$M_u = \frac{\omega L_0^2}{8} \quad (6)$$

where  $\omega$  is the distributed load along the member length  $L_0$ ,  $\omega = P/L_0$ . For unbraced Zee sections, the vertical load causes unsymmetric bending stresses at midspan, therefore the bending stresses were resolved into moments about both major and minor principal axes,  $M_1$  and  $M_2$ . The ultimate moments  $M_{1u}$  and  $M_{2u}$  thus were calculated by Eqs. 7 and 8, respectively:

$$M_{1u} = \frac{\omega L_0^2 \cos \theta}{8} \quad (7)$$

$$M_{2u} = \frac{\omega L_0^2 \sin \theta}{8} \quad (8)$$

where  $\theta$  is the acute angle between the major principal axis and the x-x geometric axis.

The ultimate bimoment  $B_u$  was calculated by Eq. 9 for both unbraced Cee and Zee sections:

$$B_u = \frac{Pe a^2}{L} \cdot \left[ \sinh \left( \frac{L}{2a} \right) \cdot \tanh \left( \frac{L}{2a} \right) + 1 - \cosh \left( \frac{L}{2a} \right) \right] \quad (9)$$

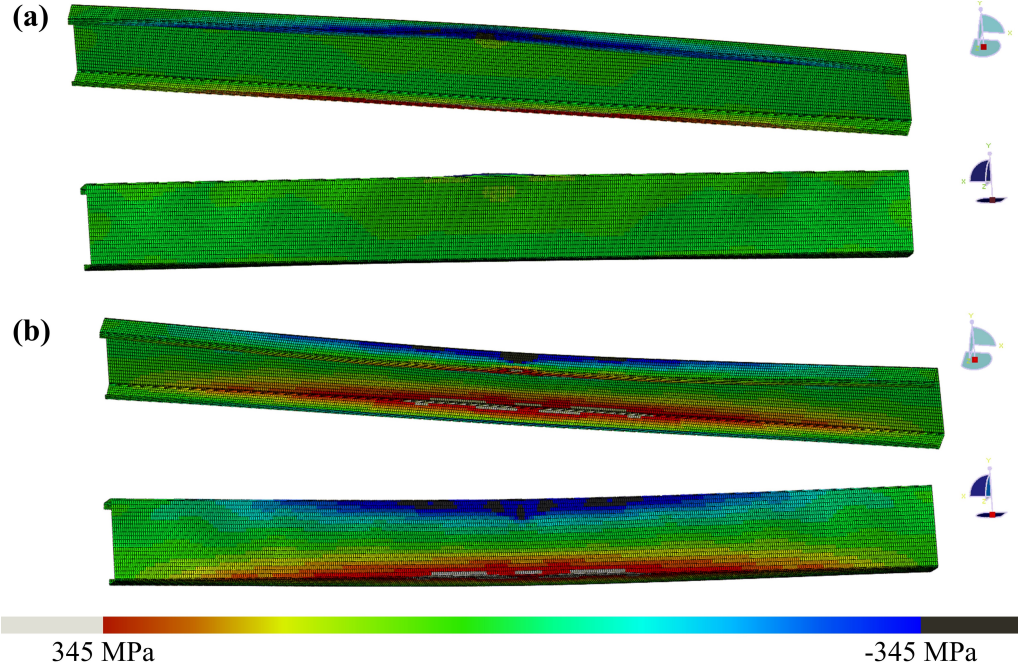


Figure 6: Representative S11 distribution of unbraced Cee section (800S250x97) with (a)  $e_3 = -B/2$  and (b)  $e_7 = +B/2$  at ultimate load.

where  $L$  is the unbraced length and equals the total member length, and  $a$  is a constant calculated by Eq. 10:

$$a = \sqrt{\frac{EC_w}{GJ}} \quad (10)$$

where  $C_w$  is torsional warping constant of cross-section,  $G$  is the shear modulus,  $G = E/(2 + 2\nu)$ , and  $J$  is the Saint-Venant torsion constant.

For the braced scenario of both Cee and Zee sections, the ultimate moment  $M_u$  was calculated by Eq. 6 and the ultimate bimoment  $B_u$  was calculated by Eq. 11:

$$B_u = -\frac{Pe a^2}{L} \cdot \left[ \cosh\left(\frac{L}{a}\right) - 1 + \left( \frac{\cosh\left(\frac{L}{a}\right) - 1 + \frac{L^2}{2a^2} - \frac{L}{a} \cdot \sinh\left(\frac{L}{a}\right)}{\frac{L}{a} \cdot \cosh\left(\frac{L}{a}\right) - \sinh\left(\frac{L}{a}\right)} \right) \cdot \sinh\left(\frac{L}{a}\right) \right] \quad (11)$$

where  $L$  is the unbraced length which is equal to half of the total member length, and  $a$  is calculated by Eq. 10.

The second method for  $M_u$  and  $B_u$  calculations is a stress-based method and it directly uses the nodal longitudinal stresses S11 of midspan nodes at peak applied load following Eq. 12, 13, and 14:

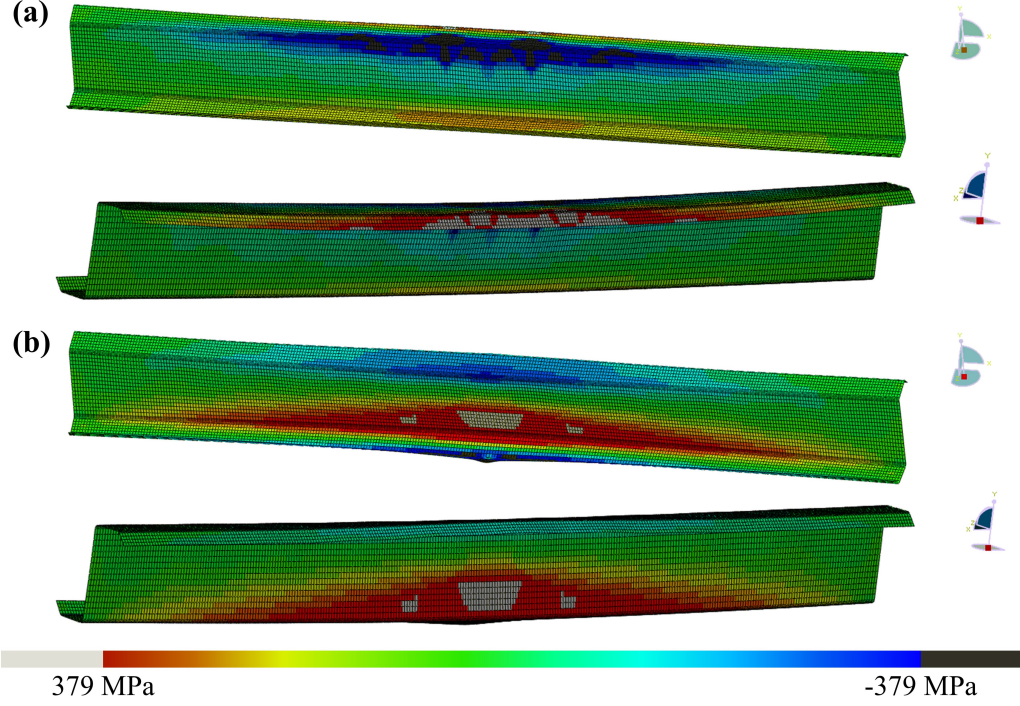


Figure 7: Representative S11 distribution of unbraced Zee section (6Z225x105) with (a)  $e_1 = -B$  and (b)  $e_9 = +B$  at ultimate load.

$$M_{xu} = \int \sigma y dA \quad (12)$$

$$M_{yu} = \int \sigma x dA \quad (13)$$

$$B_u = \int \sigma w_n dA \quad (14)$$

where the subscript  $x$  and  $y$  represent  $x-x$  and  $y-y$  geometric axes. In addition, for the unbraced Cee section,  $M_u = M_{xu}$ ; for the unbraced Zee section, the ultimate moment  $M_{1u}$  and  $M_{2u}$  are calculated by Eq. 15 and 16:

$$M_{1u} = +M_{xu} \cos \theta + M_{yu} \sin \theta \quad (15)$$

$$M_{2u} = -M_{xu} \sin \theta + M_{yu} \cos \theta \quad (16)$$

For both braced Cee and Zee sections,  $M_u = M_{xu}$ . The nominal moment capacity  $M_n$  ( $M_{1n}$  and  $M_{2n}$  for unbraced Zee sections) was calculated following Ch. F3 and F4 of AISI S100 (2020) for LB- and DB-controlled cases respectively. The bimoment capacity  $B_n$  was calculated by Eq. 5

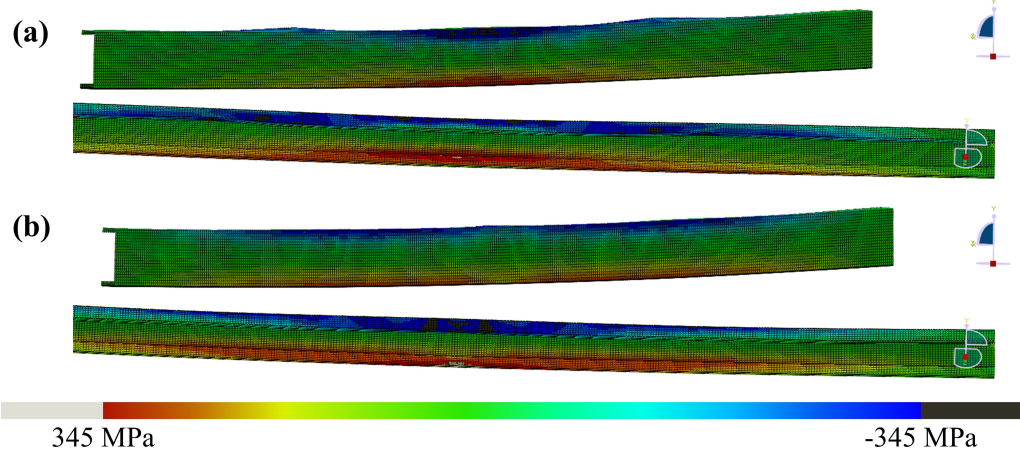


Figure 8: Representative S11 distribution of braced Cee section (800S250x68) with (a)  $e_3 = -B/2$  and (b)  $e_7 = +B/2$  at ultimate load.

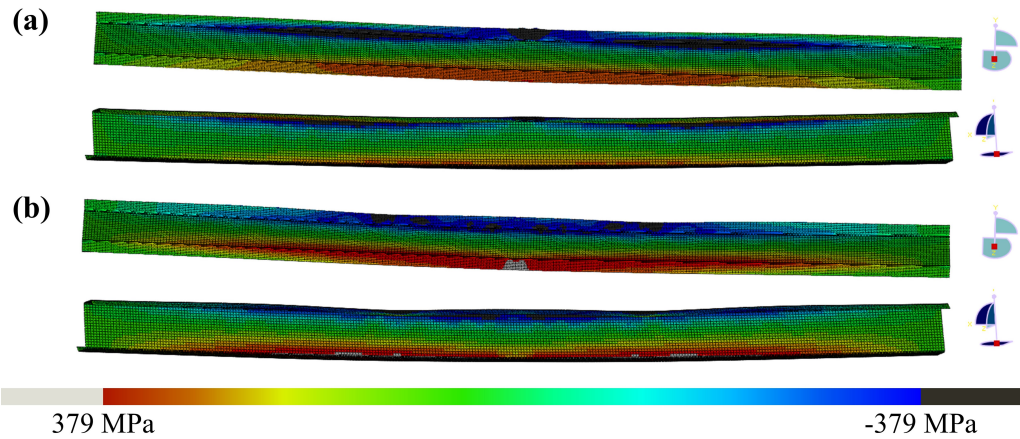


Figure 9: Representative S11 distribution of braced Zee section (6Z225x070) with (a)  $e_1 = -B$  and (b)  $e_9 = +B$  at ultimate load.

as described in the torsion-only study (Xia et al., 2022) with proposed coefficients for LB- and DB-controlled cases respectively.

## 5. Bending-torsion interaction

Based on the moment and bimoment parameters calculated in Sec. 4., the bending-torsion interaction relationship for unbraced and braced cases were developed separately. The relationship between  $B_u/B_n$  and  $M_u/M_n$  for unbraced Cee sections is shown in Fig. 10. The figure shows that the interaction is dependent on the direction of the eccentricity. For the negative eccentricities, the bimoments are positive following the CUFSM (2010) sign convention (the same hereinafter) and  $M_u/M_n + B_u/B_n$  is between 0.8 and 1.0. For the positive eccentricities, the bimoments are negative and are generally above  $M_u/M_n - B_u/B_n = 1.3$ . The relationship between  $B_u/B_n$  versus  $M_{1u}/M_{1n}$  versus  $M_{2u}/M_{2n}$  for unbraced Zee sections is shown Fig. 11. Unbraced Zee sections with both positive and negative eccentricities show substantially conservative interaction behaviors, where all the data are strictly above  $M_{1u}/M_{1n} + M_{2u}/M_{2n} + B_u/B_n = 1.3$  for the cases

with negative eccentricities and below  $M_{1u}/M_{1n} + M_{2u}/M_{2n} - B_u/B_n = 1.3$  for the cases with positive eccentricities. For both unbraced Cee and Zee sections, the positive eccentricity cases are more conservative than the negative eccentricity cases.

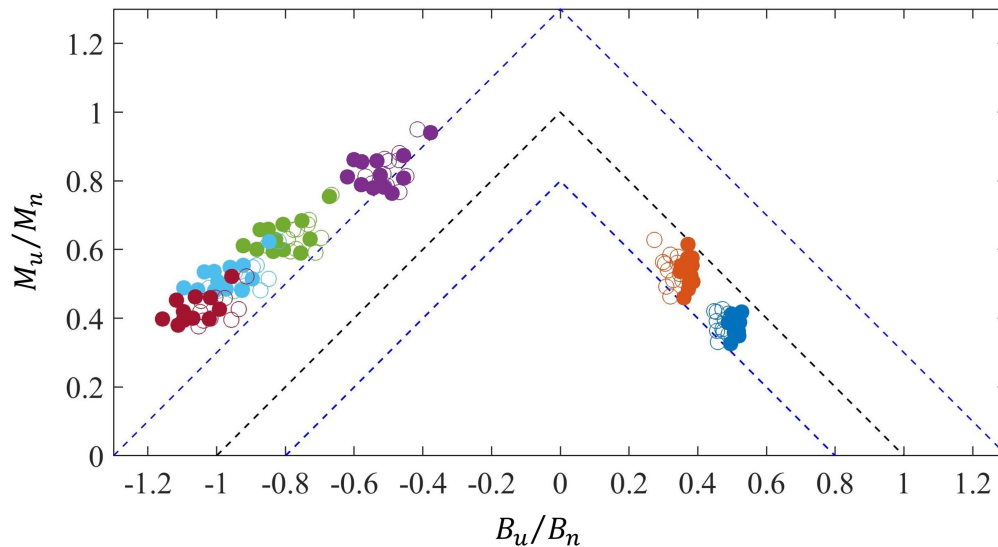


Figure 10: Interaction between  $B_u/B_n$  and  $M_u/M_n$  for unbraced Cee sections. Different colors represent different eccentricities as shown in Fig. 3(a). Solid scatters represent stress-based method and hollow ones represent equation-based method.

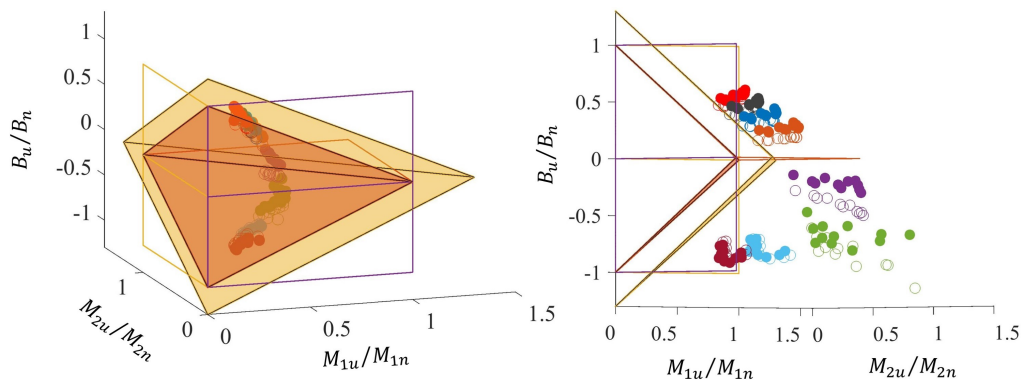


Figure 11: Interaction among  $B_u/B_n$  versus  $M_{1u}/M_{1n}$  versus  $M_{2u}/M_{2n}$  for unbraced Zee sections from two perspectives. Different colors represent different eccentricities as shown in Fig. 3(b). Solid scatters represent stress-based method and hollow ones represent equation-based method. The reference planes of  $M_{1u}/M_{1n} + M_{2u}/M_{2n} \pm B_u/B_n = 1.0$  and  $M_{1u}/M_{1n} + M_{2u}/M_{2n} \pm B_u/B_n = 1.3$  are represented by the orange and yellow shaded areas, respectively.

For the braced cases, the Cee and Zee sections show similar interaction behaviors between  $B_u/B_n$  versus  $M_u/M_n$  as shown in Fig. 12. While significantly different behaviors are observed among positive and negative eccentricity cases. The negative eccentricity cases show negative bimoments and the data is generally above  $M_u/M_n - B_u/B_n = 1$ . In contrast, the positive eccentricity cases show positive bimoments and the data is more conservative and generally above  $M_u/M_n + B_u/B_n = 1.2$ .

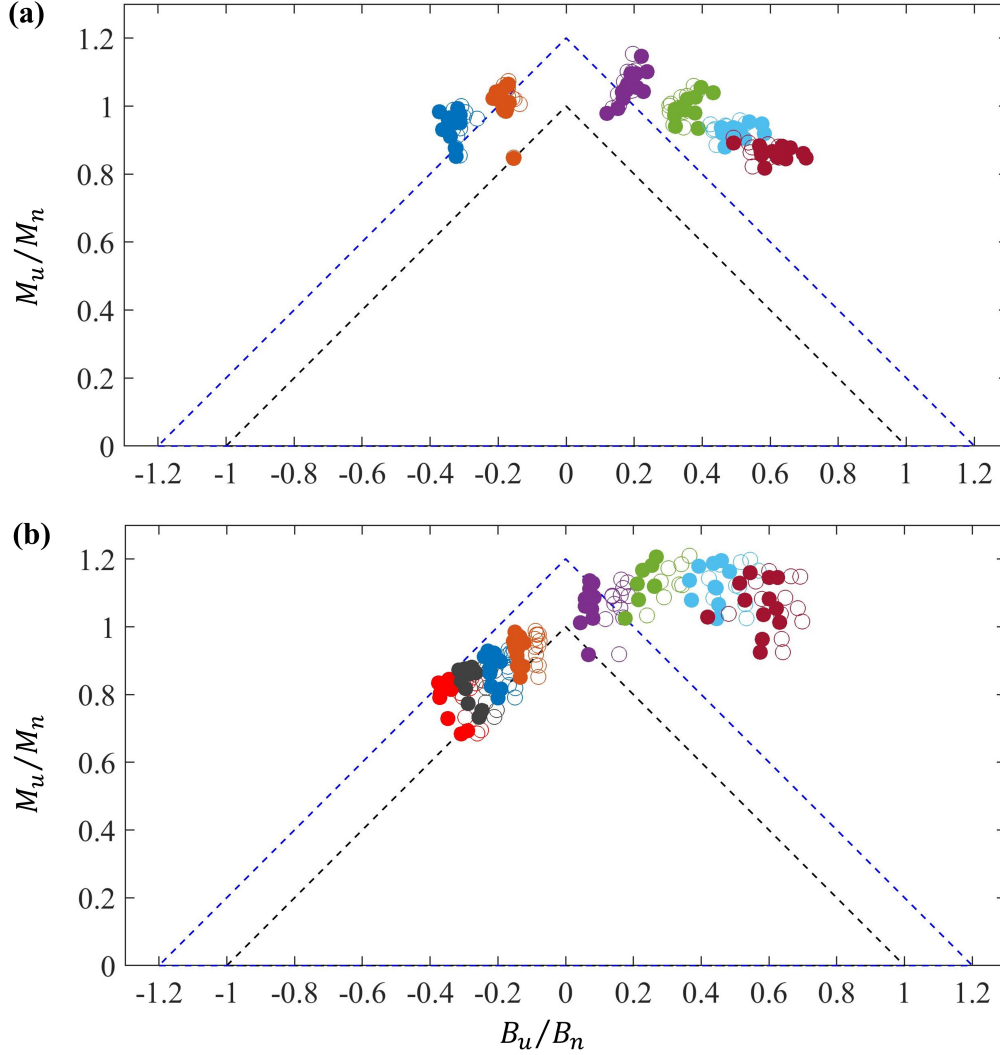


Figure 12: Interaction between  $B_u/B_n$  and  $M_u/M_n$  for braced (a) Cee and (b) Zee sections. Different colors represent different eccentricities as shown in Fig. 3. Solid scatters represent stress-based method and hollow ones represent equation-based method.

## 6. Conclusions

The moment-bimoment interaction equations have been developed in this study. A set of moment and bimoment parameters, including nominal moment capacity  $M_n$ , ultimate moment  $M_u$ , nominal bimoment capacity  $B_n$ , and ultimate bimoment  $B_u$ , incorporated in the interaction equation were calculated using a validated finite element model for CFS Cee and Zee sections under combined bending-torsion considering buckling and/or inelastic behaviors. A wide range of practical cross-sections, loading eccentricities, and two different bracing conditions at midspan were investigated. The results indicated that both the direction of the loading eccentricity and the midspan bracing have significant effects on the member behaviors and interaction equation prediction. The direction of the loading eccentricity and the midspan bracing determine the sign of  $B_u$ , where positive  $B_u$  for unbraced cases and negative  $B_u$  for braced cases are observed in the negative load eccentricity scenarios, and reversed signs are observed in the positive eccentricity scenarios. Furthermore, the

moment-bimoment interactions for most cases are generally above  $M_u/M_n + |B_u|/B_n = 1.2$  or 1.3 (or  $M_{1u}/M_{1n} + M_{2u}/M_{2n} + B_u/B_n = 1.2$  for unbraced Zee sections), indicating the behaviors are conservative compared with design standards. The exceptions are the unbraced Cee section and braced Zee section cases loaded with negative eccentricities, where  $M_u/M_n + |B_u|/B_n$  is between 0.8 and 1.0. This study indicates the need to revise moment-bimoment predictions in applicable CFS design specifications.

## References

- Abaqus (2016). *version 6.16*. Dassault Systèmes Simulia Corp.
- American Iron and Steel Institute (2020). *S100-16 (R2020): North American Specification for the Design of Cold-formed Steel Structural Members*. Washington, DC, U.S.A.
- American Iron and Steel Institute (AISI) (2017). *D100-17: AISI Manual Cold-Formed Steel Design*. Washington, DC, U.S.A.
- European Committee for Standardization (CEN) (2006). *Eurocode 3: Design of steel structures, Part 1-3: General rules - Supplementary rules for cold-formed members and sheeting*. Brussels, Belgium, pp. 1–130.
- Glauz, Robert S. (2020). “Torsion Analysis for Cold-Formed Steel Members Using Flexural Analogies”. In: *Proceedings of the Cold-Formed Steel Research Consortium Colloquium*. URL: <http://jhir.library.jhu.edu/handle/1774.2/63139>.
- Glauz, Robert S. and Benjamin W. Schafer (Apr. 2022). “Modifications to the Direct Strength Method of cold-formed steel design for members unsymmetric about the axis of bending”. In: *Thin-Walled Structures* 173, p. 109025. ISSN: 0263-8231. DOI: 10.1016/j.tws.2022.109025.
- Li, Zhanjie and Benjamin W. Schafer (2010). “Buckling Analysis of Cold-formed Steel Members with General Boundary Conditions Using CUFSM Conventional and Constrained Finite Strip Methods”. In: *CCFSS Proceedings of International Specialty Conference on Cold-Formed Steel Structures (1971 - 2018)*. St. Louis, Missouri, U.S.A.
- Ministry of Construction of the P.R.C and General Administration of Quality Supervision, Inspection and Quarantine of the P.R.C (2002). *Technical code of cold-formed thin-wall steel structures*. Beijing, China, pp. 1–93.
- Steel Stud Manufacturers Association (SSMA) (2015). *SSMA Product Technical Guide*. Boise, ID, U.S.A.
- Wan, Hong Xia, Bin Huang, and Mahen Mahendran (2021). “Experiments and numerical modelling of cold-formed steel beams under bending and torsion”. In: *Thin-Walled Structures* 161, p. 107424. ISSN: 02638231. DOI: 10.1016/j.tws.2020.107424.
- Xia, Yu et al. (2022). “Cold-formed steel strength predictions for torsion”. In: *Proceedings of the Annual Stability Conference*. Denver, Colorado, U.S.A., pp. 1–16.